Supplementary Information for
Machine learning-enabled design of architected materials

Bo Peng,Ye Wei*,Yu Qin*, Jiabao Dai, Yue Li
Aobo Liu, Tian Yun, Liuliu Han, Yufeng Zheng, Peng Wen*
*Corresponding author. E-mail: weiye@mail.tsinghua.edu.cn,
qinyu95@126.com, wenpeng@tsinghua.edu.cn

This pdf file includes:

Section S1 to S5

Figure S1 to S23

Table S1 and S5

References (1-16)

S1. Model performance evaluation

The task in this study can be mathematically formulated as follows:

Find $x \in H$

To the mapping $f : H \longrightarrow Y$ and $g : H \longrightarrow E$

Such that $x = argmax_{x \in H}(f(x))$ and $g(x) = E_{target}$

Under the constraint: weight <= fixed constant

H is the scaffold design space; f and g are the mappings of scaffold design to its corresponding Y and E. Fig. 1 shows a visualization of the exploration path.

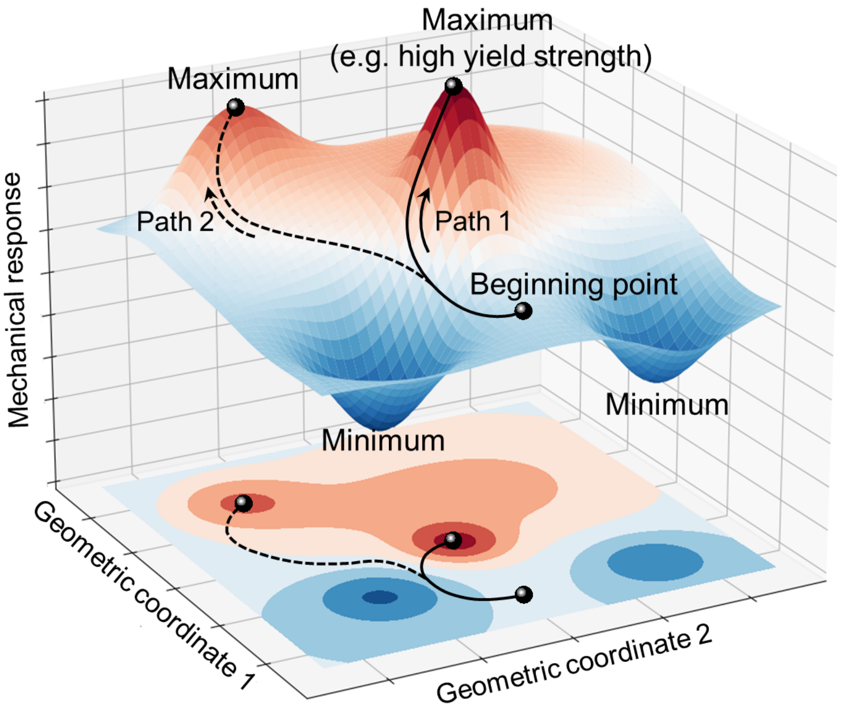

Fig. 1. Representation of the constrained multi-objective optimization task in this study. The contour surface represents the arrangement with equal E. The task is to find the maximum yield point on this surface.

Fig. 2 shows the training history of 3D-CAE with eight latent dimensions. The loss quickly dropped to near zero after 60 epochs. The histogram (inlet) shows that the loss of 4-dimension latent space was high, while sampling from the 16-dimension was time-consuming. 8-dimension reached a balance between loss and efficiency.

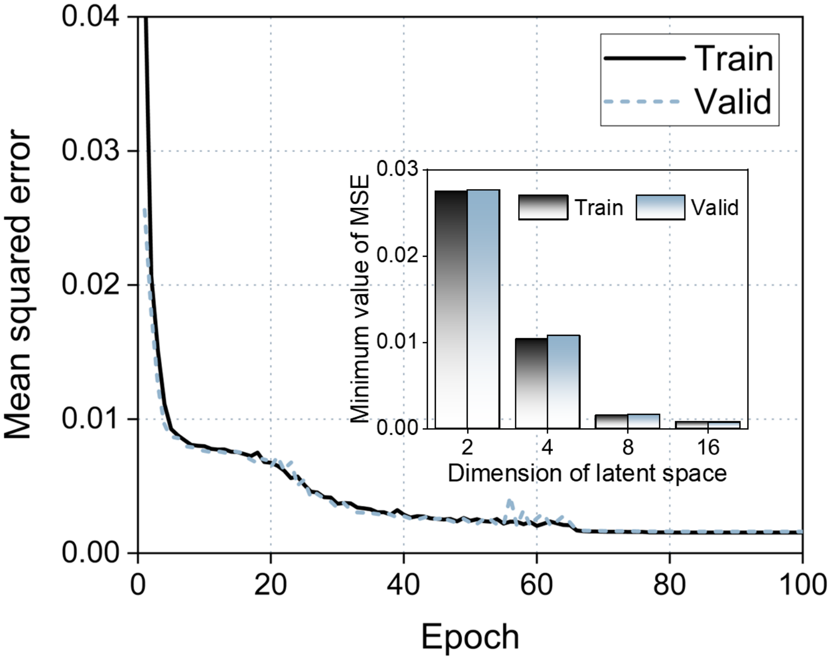

Fig. 2. Training of 3D-CAE. Training history of 3D-CAE. The loss reaches almost zero after 60 epochs; inlet shows the histogram of the loss v.s. the latent space dimension.

Fig. 3 and 4 demonstrate the performance evaluation of 3D-CNNs (for the E and Y) on the Ti and Zn test dataset. Both 3D-CNNs show high accuracy in the regression tasks (R^2 ratio > 0.98) at each active learning iteration. The test dataset was uniformly sampled from the labelled dataset.

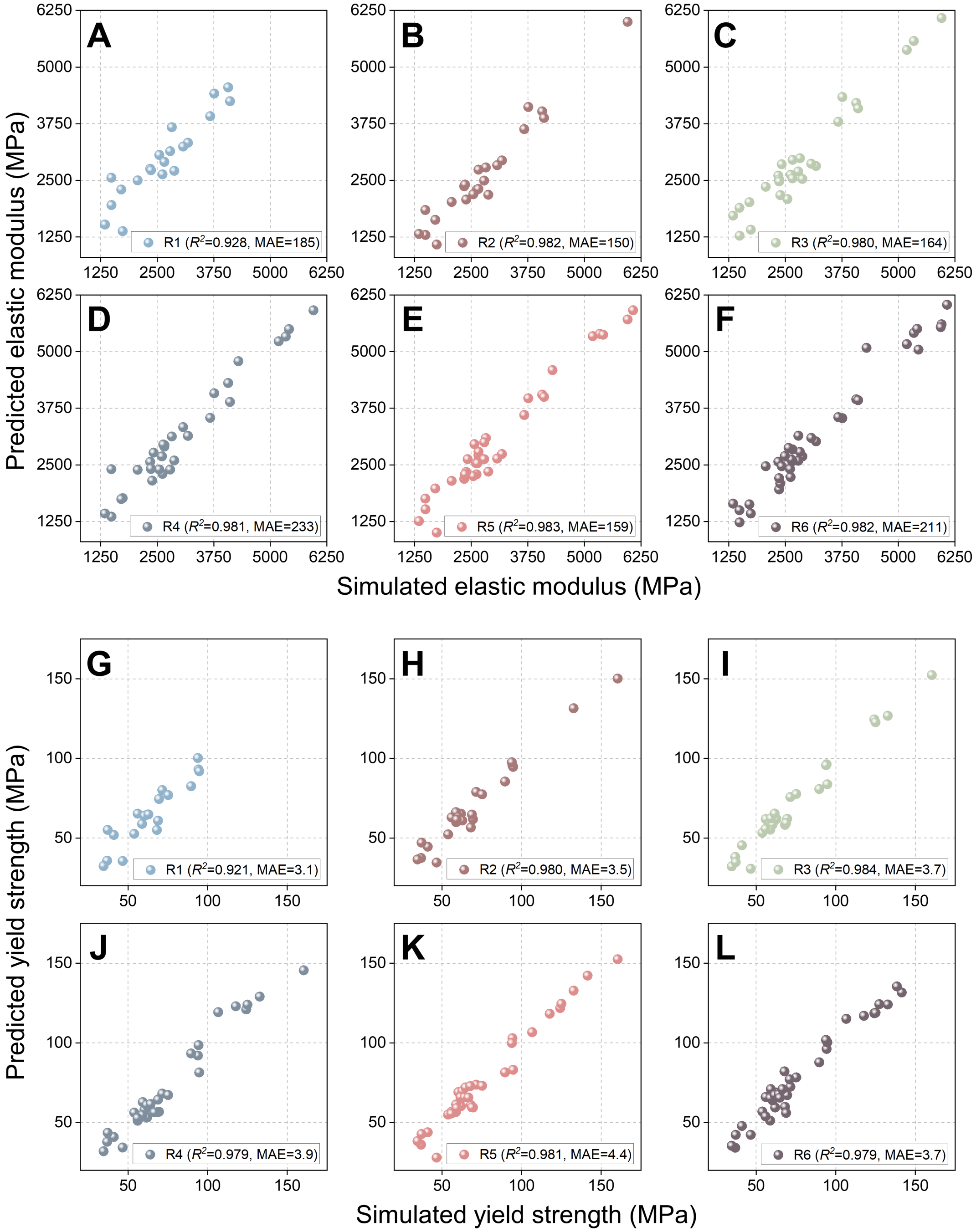

Fig. 3. Performance evaluation of 3D-CNNs on the Ti test dataset. (**A** to **L**) show the R^2 and mean average error (MAE) of 3D-CNNs from round 1 to 6, (**A** to **F**) refer to the E and (**G** to **L**) refer to the Y.

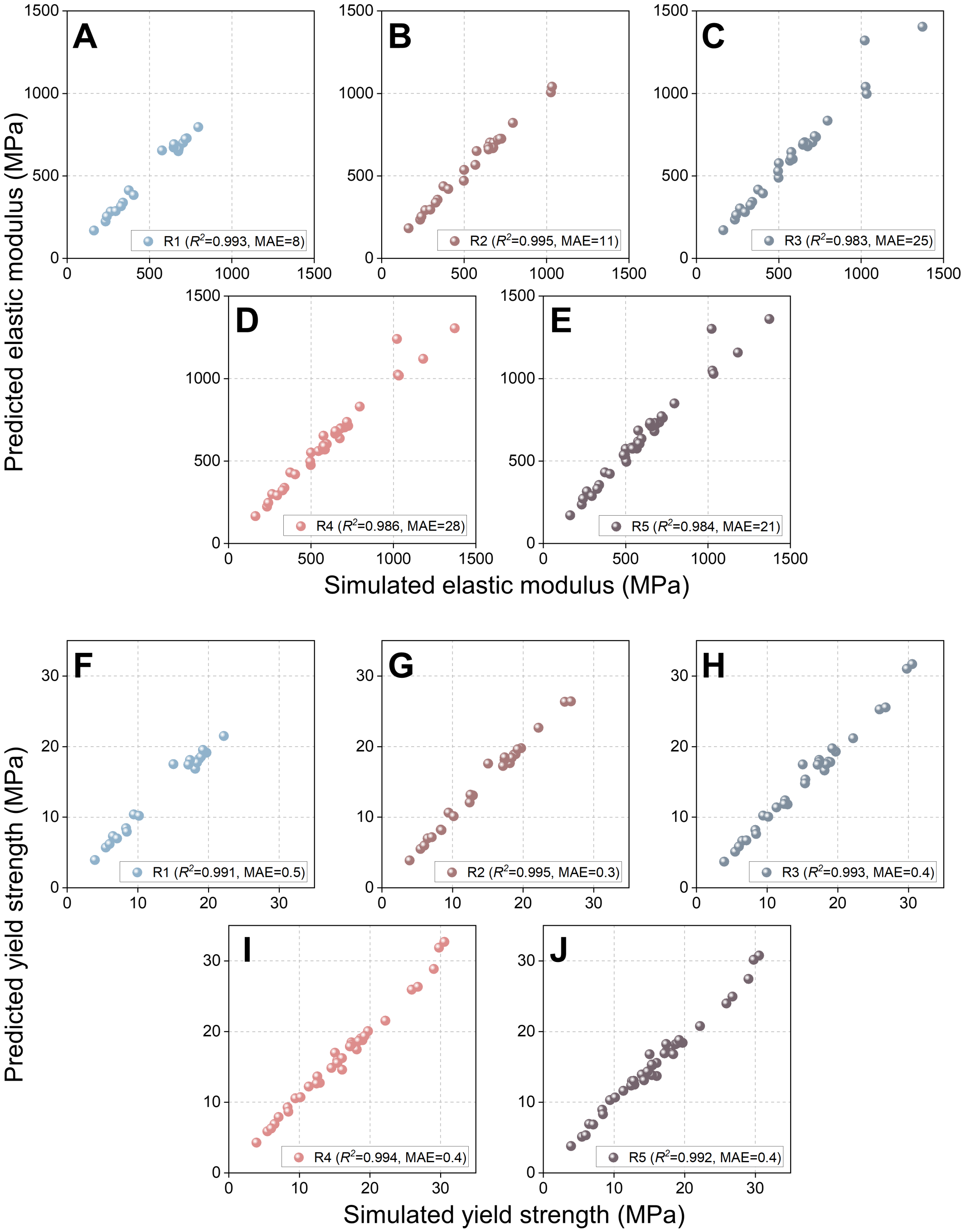

Fig. 4. Performance evaluation of 3D-CNNs on the Zn testing dataset. (**A** to **J**) show the R^2 and mean average error of 3D-CNNs from round 1 to 5, (**A** to **E**) refer to the E and (**F** to **J**) refer to the Y.

The Gaussian mixture model (GMM) was used to estimate the density in the latent z space (i.e., the marginal posterior $q_\phi(z)$). GMM is a density estimation model that uses a mixture of a finite number of Gaussian distributions with unknown mean and covariance to fit the data points. The number of Gaussian distributions is usually determined via the empirical elbow method. The elbow method is a heuristic used in determining the Pareto fronts in multi-objective optimization, in this case, it was used to determine the potential optimal number of Gaussian). As shown in Fig. 5, the average negative log-likelihood was plotted as a function of the number of Gaussian and we selected 4 as it represents the 'elbow' of the curve.

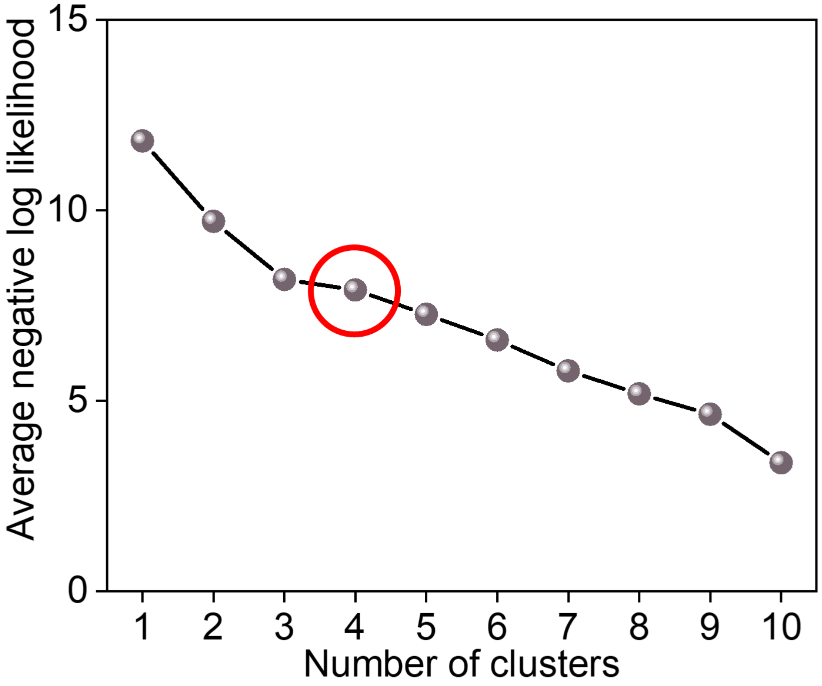

Fig. 5. The average negative log-likelihood versus the number of clusters in the GMM.

Table 1 and 2 contain the result of each learning iteration for the Ti and Zn cubic scaffolds, respectively.

Table 1 – The Ti cubic scaffolds - Mean and standard deviation of the E and Y at each iteration.

		E2500 Task			E5000 Task		
		Elastic modulus (MPa)	**Yield strength (MPa)**	**Porosity (%)**	**Elastic modulus (MPa)**	**Yield strength (MPa)**	**Porosity (%)**
Iteration	1	2311 ± 73	57.7 ± 3.3	74.1 ± 0.3	6226 ± 408	139.7 ± 11.8	57.3 ± 1.7
	2	2684 ± 69	62.6 ± 3.1	71.8 ± 0.7	5789 ± 142	136.6 ± 5.3	57.3 ± 0.3
	3	2423 ± 59	65.1 ± 5.3	70.6 ± 1.2	5526 ± 122	124.8 ± 6.8	58.5 ± 0.3
	4	2570 ± 47	66.6 ± 3.9	70.3 ± 0.7	5072 ± 147	119.1 ± 5.8	60.4 ± 0.6
	5	2686 ± 156	69.4 ± 5.2	69.6 ± 1.3	5271 ± 81	129.4 ± 9.8	57.0 ± 1.3
	6	2566 ± 47	70.0 ± 1.7	70.1 ± 0.3	5059 ± 128	136.0 ± 5.9	57.5 ± 0.9

Table 2 – The Zn cubic scaffolds - Mean and standard deviation of the E and Y at each iteration.

		E500 Task			E1000 Task		
		Elastic modulus (MPa)	**Yield strength (MPa)**	**Porosity (%)**	**Elastic modulus (MPa)**	**Yield strength (MPa)**	**Porosity (%)**
Iteration	1	546 ± 52	12.9 ± 0.8	57.9 ± 0.5	1024 ± 22	26.2 ± 0.7	45.1 ± 0.2
	2	508 ± 19	12.1 ± 0.6	59.1 ± 0.8	1297 ± 85	32.1 ± 1.3	38.0 ± 0.5
	3	568 ± 34	15.2 ± 0.9	56.7 ± 0.9	1123 ± 71	28.8 ± 0.9	41.9 ± 1.3
	4	555 ± 31	14.8 ± 0.7	56.0 ± 1.1	1024 ± 27	29.4 ± 0.3	43.2 ± 0.5
	5	515 ± 16	14.2 ± 0.7	58.9 ± 0.2	965 ± 18	28.8 ± 0.5	43.7 ± 0.1

S2. Data generation

Fig. 6 shows the schematic for the smooth transition between units with different porosity.

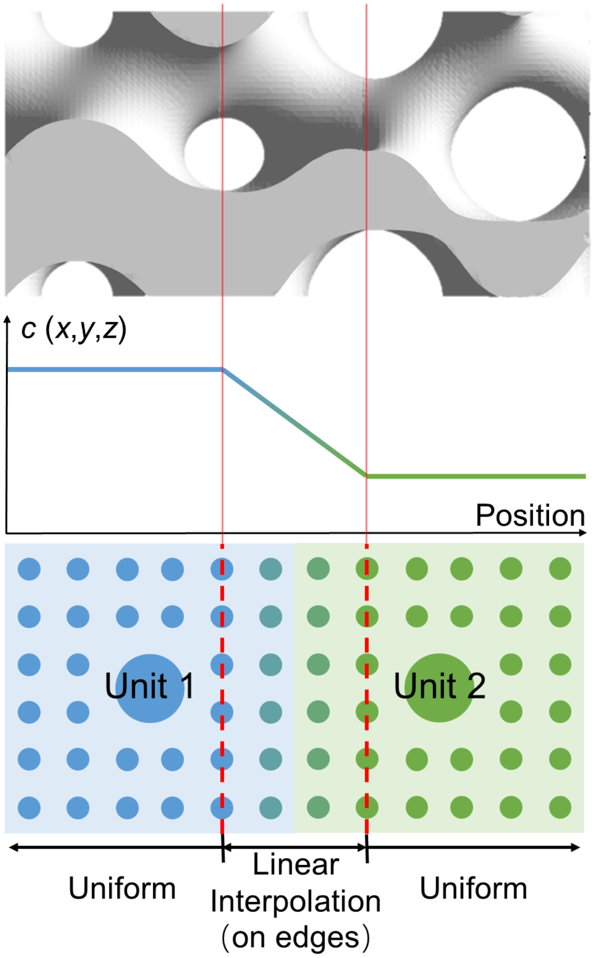

Fig. 6. The schematic for the smooth transition between units with different porosity.

Fig. 7(A and B) show the schematics for unlabelled scaffold preparation. Fig. 7(C to H) shows the simulation and experimental data of two randomly selected cubic scaffolds. ABAQUS/Explicit software was used for compression simulation (*1*).

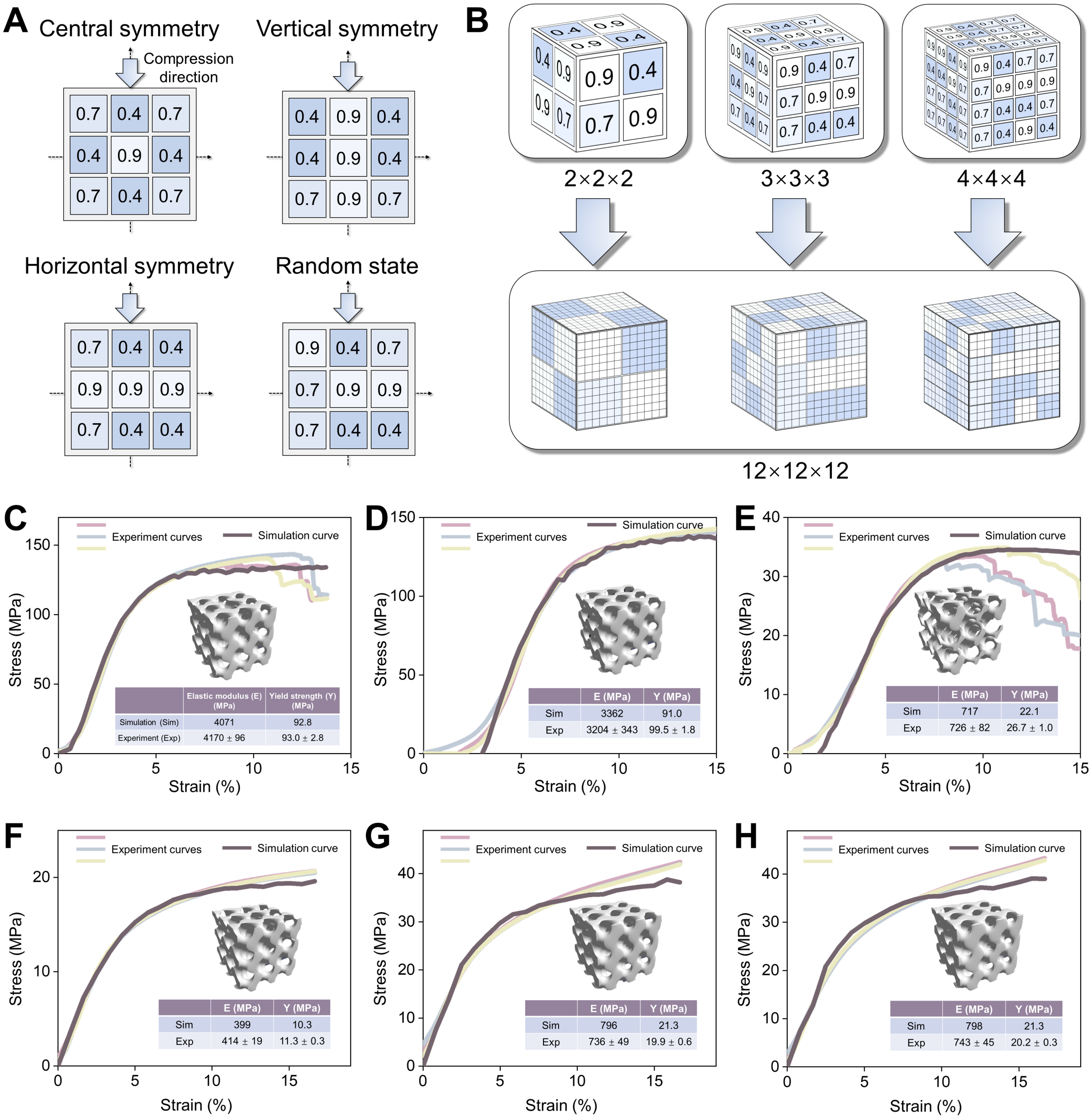

Central symmetry

0.7	0.4	0.7
0.4	0.9	0.4
0.7	0.4	0.7

Vertical symmetry

0.4	0.9	0.4
0.4	0.9	0.4
0.7	0.9	0.7

Horizontal symmetry

0.7	0.4	0.4
0.9	0.9	0.9
0.7	0.4	0.4

Random state

0.9	0.4	0.7
0.7	0.9	0.9
0.7	0.4	0.4

C

	Elastic modulus (E) (MPa)	Yield strength (Y) (MPa)
Simulation (Sim)	4071	92.8
Experiment (Exp)	4170 ± 96	93.0 ± 2.8

D

	E (MPa)	Y (MPa)
Sim	3362	91.0
Exp	3204 ± 343	99.5 ± 1.8

E

	E (MPa)	Y (MPa)
Sim	717	22.1
Exp	726 ± 82	26.7 ± 1.0

F

	E (MPa)	Y (MPa)
Sim	399	10.3
Exp	414 ± 19	11.3 ± 0.3

G

	E (MPa)	Y (MPa)
Sim	796	21.3
Exp	736 ± 49	19.9 ± 0.6

H

	E (MPa)	Y (MPa)
Sim	798	21.3
Exp	743 ± 45	20.2 ± 0.3

Fig. 7. Data generation and simulation calibration. (**A**) The porosity matrix database contains three symmetries and one random arrangement. (**B**) Three kinds of porosity matrices: $2*2*2$, $3*3*3$ and $4*4*4$, which can all expand to a $12*12*12$ matrix. The $3*3*3$ arrangement was chosen to balance structural complexity and computational efficiency. (**C** to **H**) The FEM simulation agrees with experimental observations. Three replicas were tested in order to ensure reproducibility. The error of the E and Y between FEM simulation and experimental results is less than 10%. (C to E) refer to 3 Ti scaffolds with random shapes, and (F to H) refer to 3 Zn scaffolds with random shapes. (C to H) All stress-strain curves are adjusted in the x-axis direction to make them overlap.

S3. FEM analysis of cubic scaffolds

This section discusses the detailed FEM analysis of ML design cubic scaffolds from E2500 (Ti), E5000 (Ti), and E1000 (Zn) tasks.

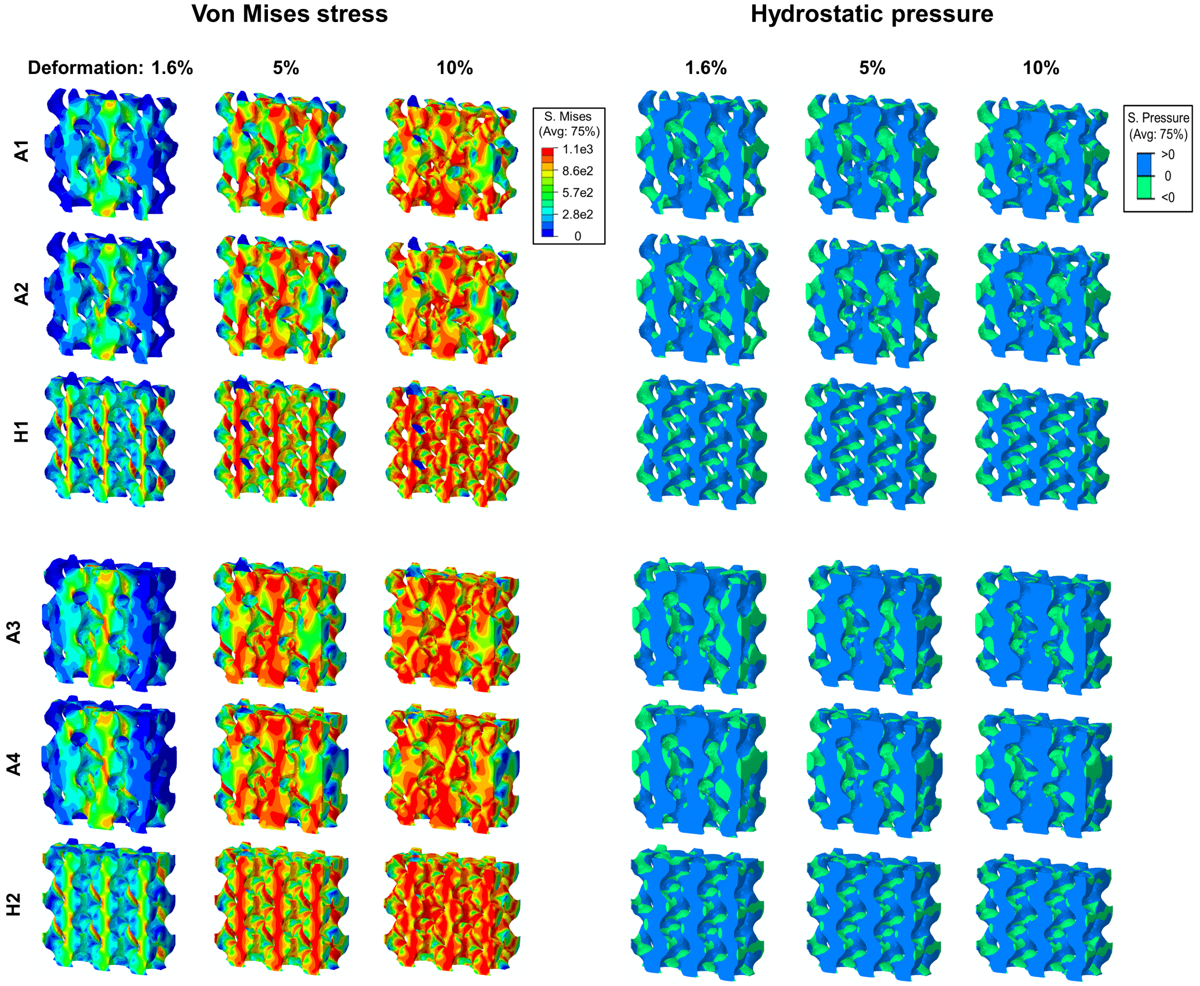

Fig. 8. FEM analysis of the Ti cubic scaffolds. Numerical compression analysis of Von-Mises stress and hydrostatic pressure under 1.6%, 5%, 10% deformation. The cross-section view of ML designs (A1-A4) and expert designs (H1 and H2) is plotted.

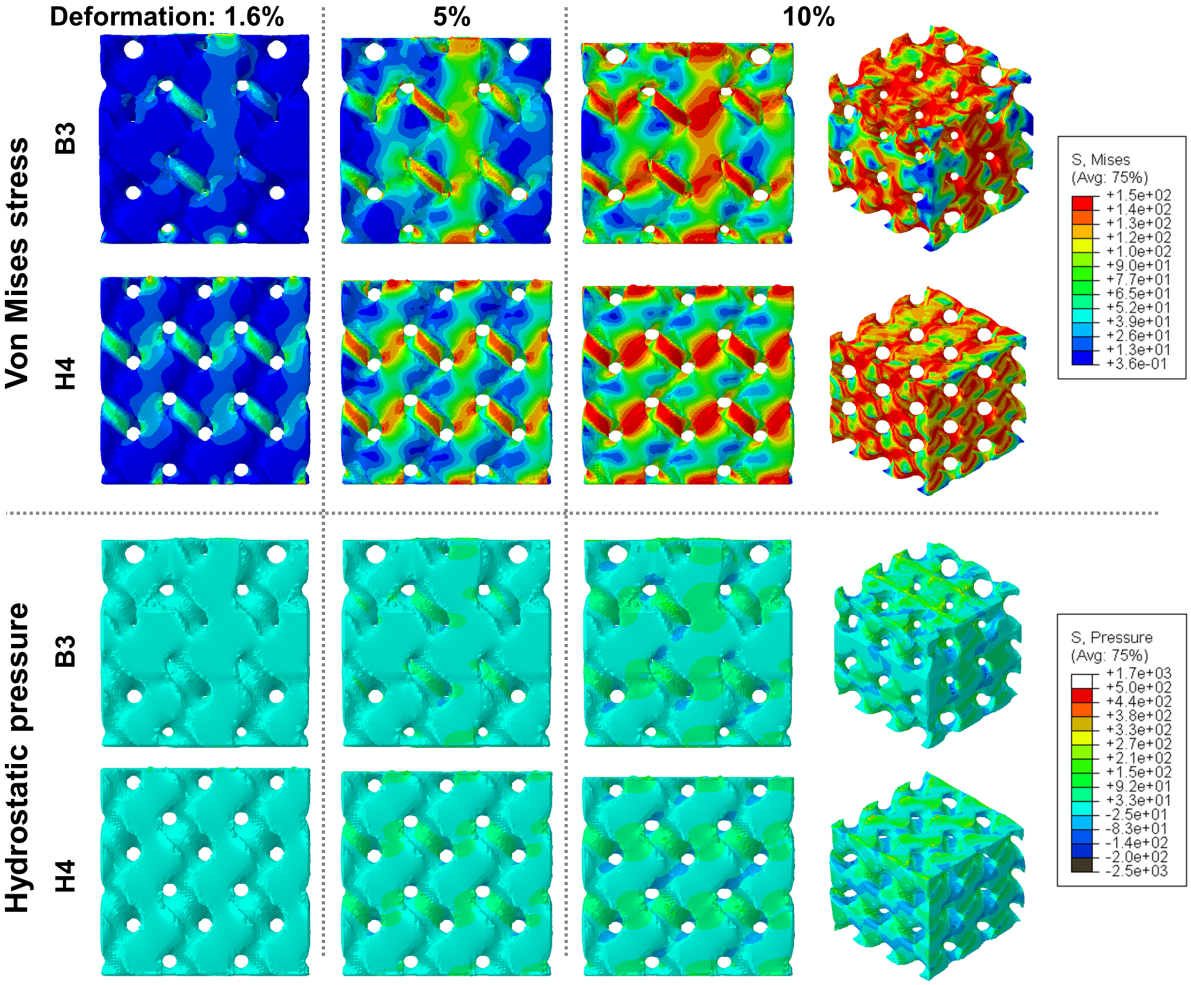

Fig. 9. FEM analysis of the Zn cubic scaffolds. Numerical compression analysis of Von-Mises stress and hydrostatic pressure under 1.6%, 5%, 10% deformation. The front and orthographic views of ML design (B3) and expert design (H4) are plotted.

S4. Experimental characterization of cubic-shaped scaffolds

Table 3 – Experimental result of ML design and expert design Ti cubic scaffold. A1(2) and A3(4) represent the best candidates for E2500 and E5000 tasks, respectively. Expert design (uniform) H1 and H2 are the reference scaffolds of E2500 and E5000.

	A1	A2	H1	A3	A4	H2
Elastic modulus (MPa)	2527 ± 87	2649 ± 195	2627 ± 154	5169 ± 422	4947 ± 450	4903 ± 303
Yield strength (MPa)	74.8 ± 2.2	73.4 ± 1.9	60.0 ± 1.1	147.6 ± 4.2	147.2 ± 2.3	119.8 ± 8.6
Porosity (%)	69.3 ± 0.3	69.1 ± 0.1	73.0 ± 0.2	57.5 ± 0.3	55.6 ± 0.1	60.8 ± 0.3

Table 4 – Experimental result of ML design and expert design Zn cubic scaffolds. B1(2) and B3(4) represent the best candidates from E500 tasks and E1000, respectively. H3(4) are the reference scaffolds (uniform porosity) of E500 and E1000. B3 scaffold shows superior performance over the gold criteria H4 scaffold.

	B1	B2	H3	B3	B4	H4
Elastic modulus (MPa)	484 ± 17	510 ± 28	510 ± 28	1066 ± 35	1012 ± 22	975 ± 19
Yield strength (MPa)	13.0 ± 0.6	12.7 ± 0.3	12.9 ± 0.5	26.4 ± 0.7	21.8 ± 0.7	21.7 ± 1.8
Porosity (%)	56.5 ± 0.5	56.8 ± 0.2	55.8 ± 0.1	35.4 ± 0.2	38.6 ± 0.1	39.3 ± 0.4

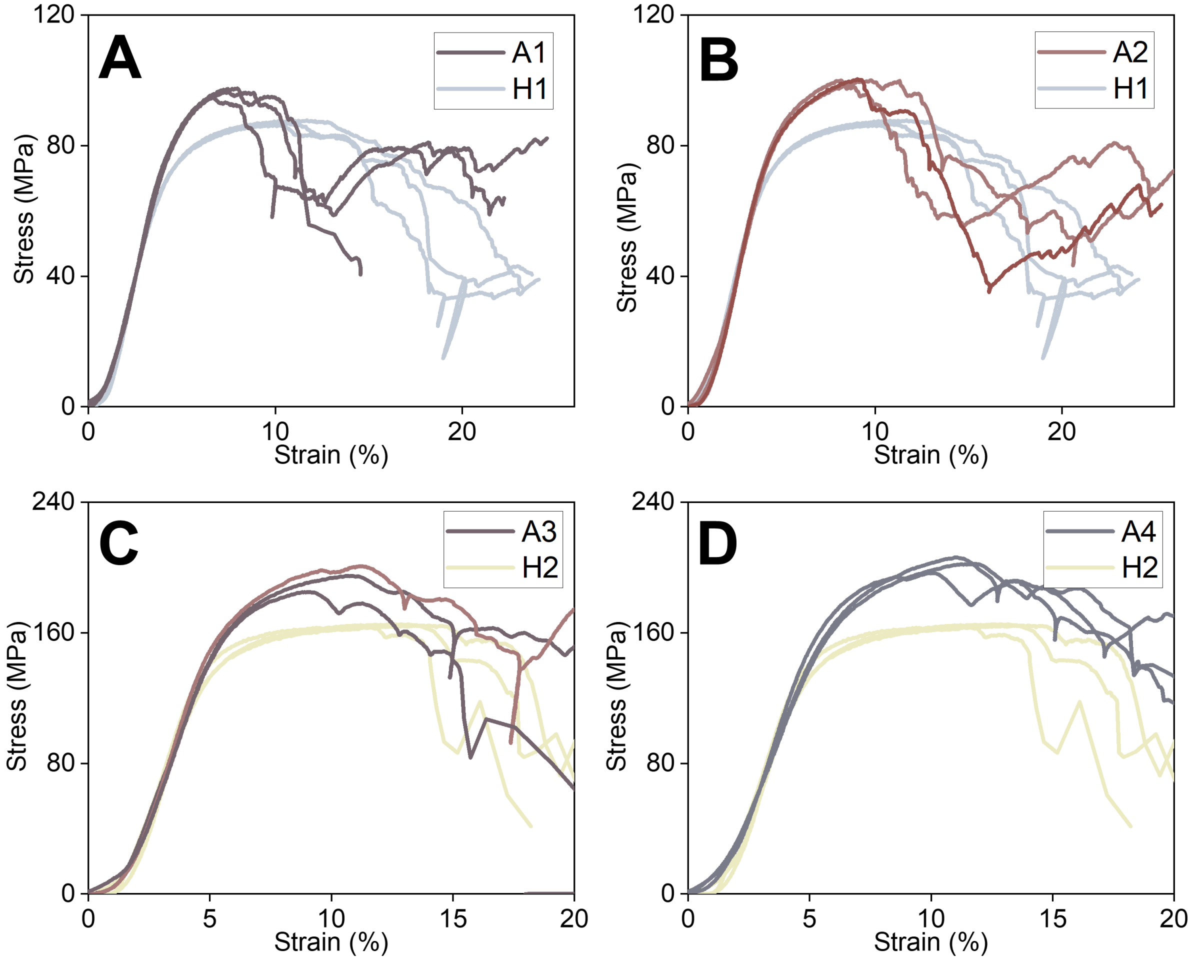

Fig. 10. Compression test curves of the Ti cubic scaffolds. ML designs (A1-A4) and expert designs (H1 and H2). Three replicas were tested in order to ensure reproducibility. In each figure, all stress-strain curves are adjusted in the x-axis direction to make them overlap.

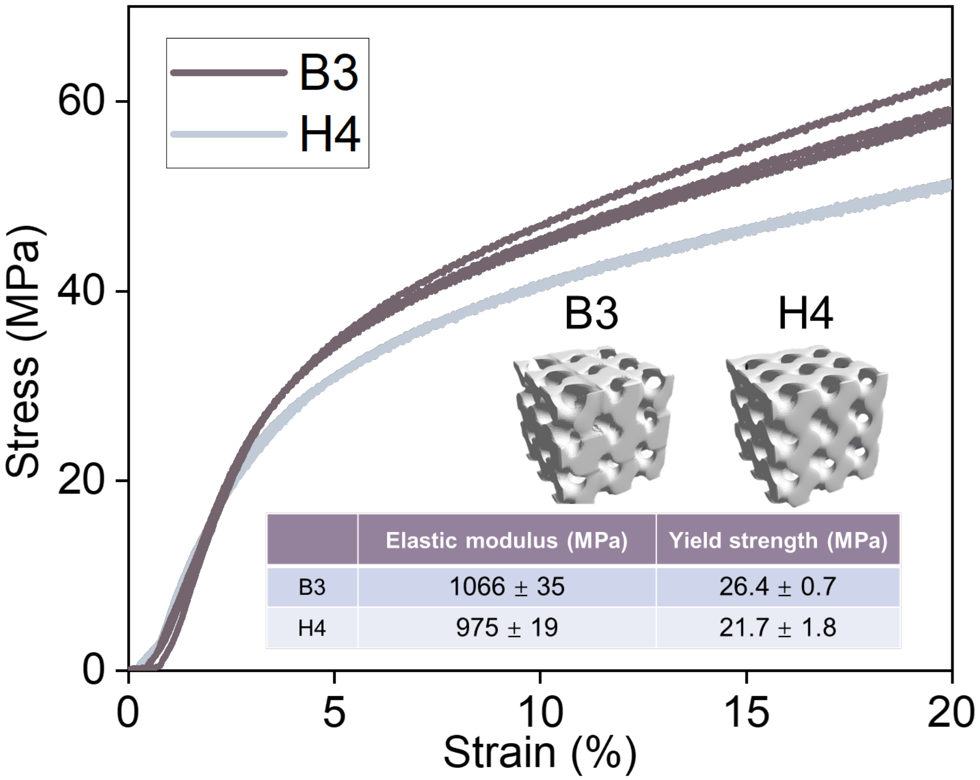

	Elastic modulus (MPa)	Yield strength (MPa)
B3	1066 ± 35	26.4 ± 0.7
H4	975 ± 19	21.7 ± 1.8

Fig. 11. Experimental strain-stress curves of the Zn cubic scaffolds. ML design (B3) and expert design (H4). Three replicas were tested in order to ensure reproducibility. In each figure, all stress-strain curves are adjusted in the x-axis direction to make them overlap.

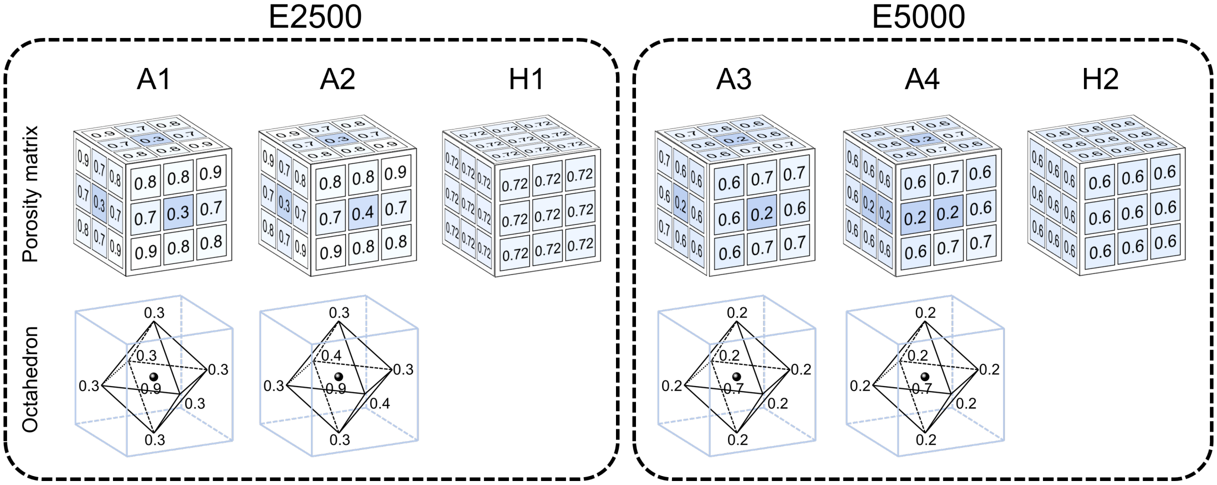

Fig. 12. The porosity matrices and ’face-centered’ lattice structures of the Ti cubic scaffolds. The porosity matrices of ML designs (A1-A4) and expert designs (H1 and H2). The ’face-centered’ lattice structures of ML designs (A1-A4).

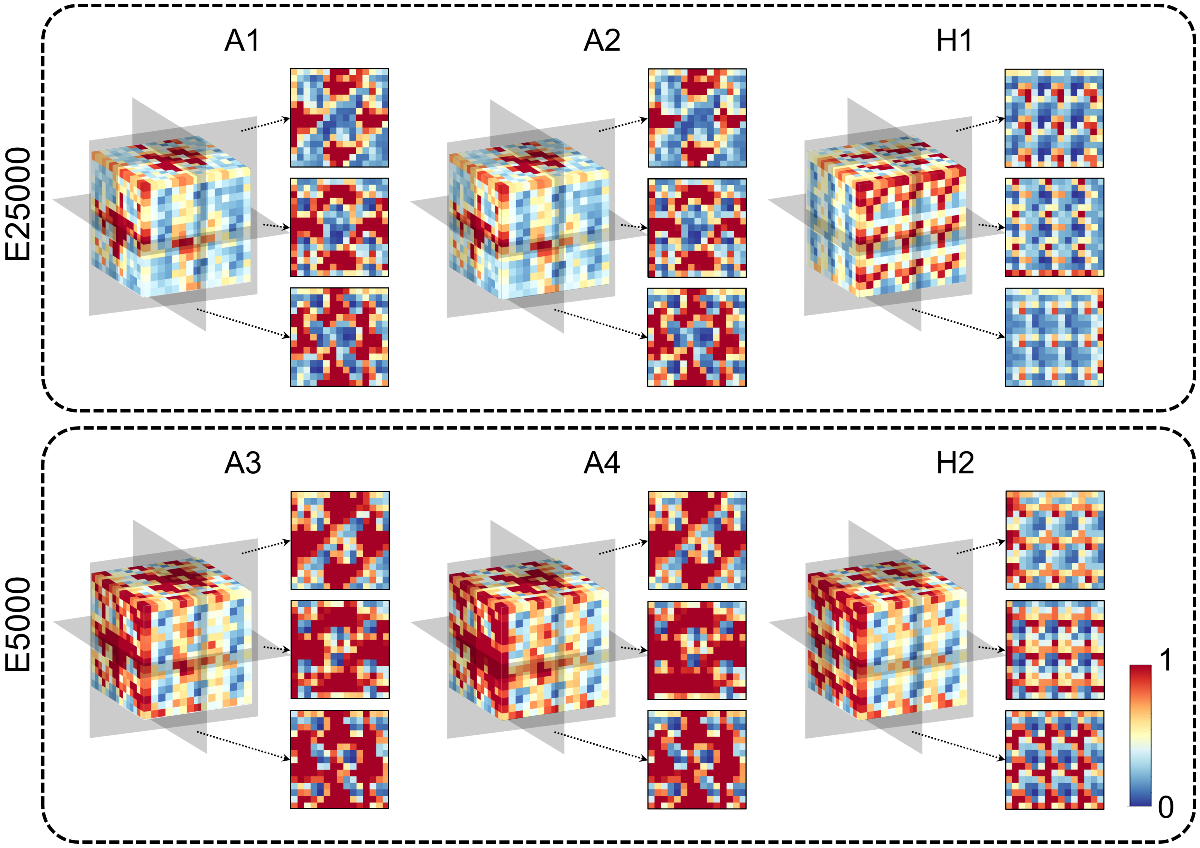

Fig. 13. Regression activation map of the Ti cubic scaffolds. The x-z, x-y, and y-z cross sections of the RAM of ML designs (A1-A4) and expert designs (H1 and H2).

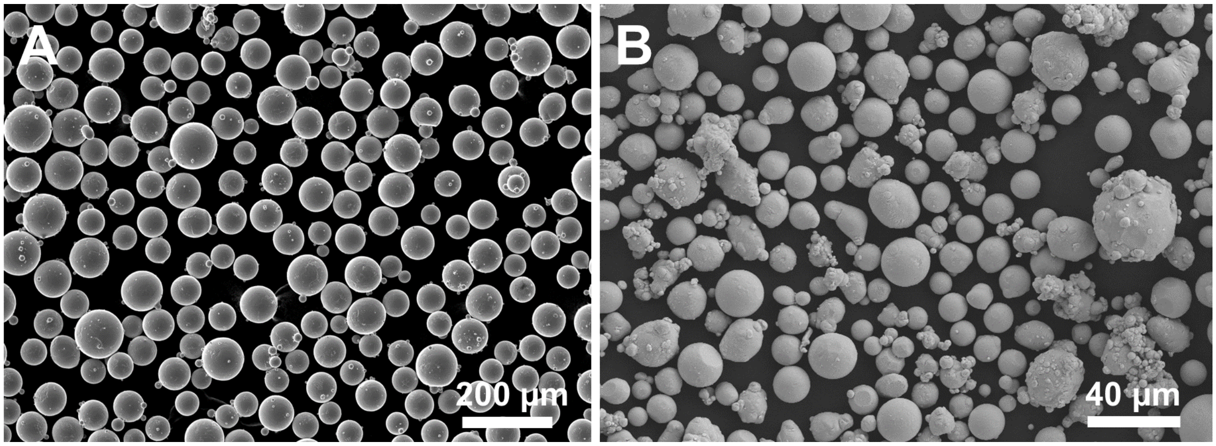

Fig. 14. Powder observation. (**A**) The Ti powder. (**B**) The Zn powder.

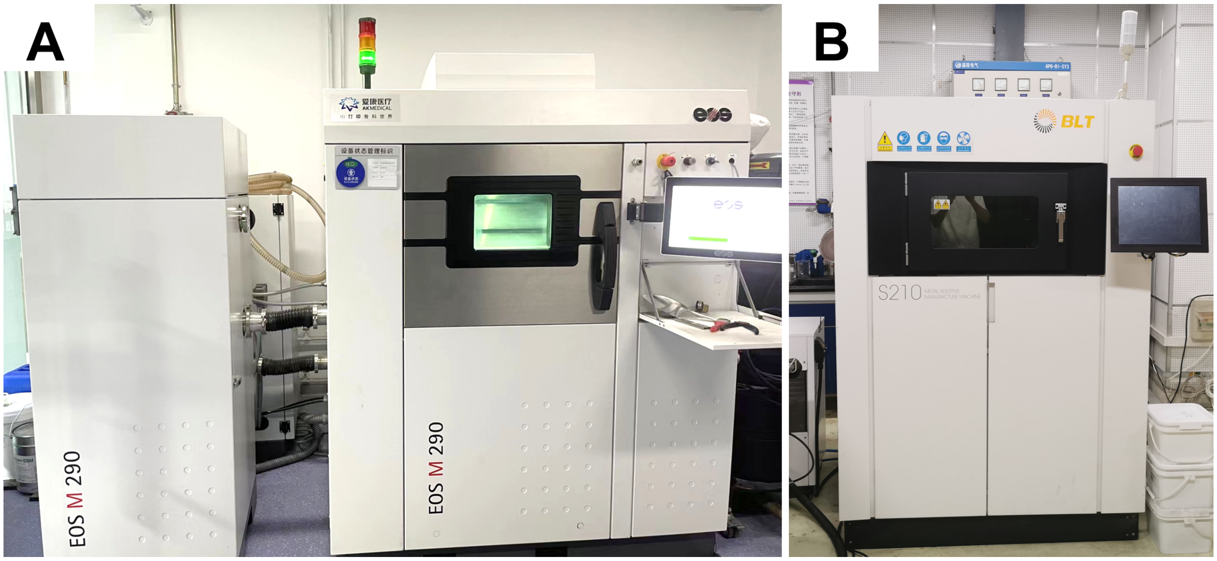

Fig. 15. Laser powder bed fusion machines of the Ti and Zn cubic scaffolds. (**A**) The EOS M290 machine used for additively manufacturing the Ti cubic scaffolds. (**B**) The BLT S210 machine used for manufacturing the Zn cubic scaffolds.

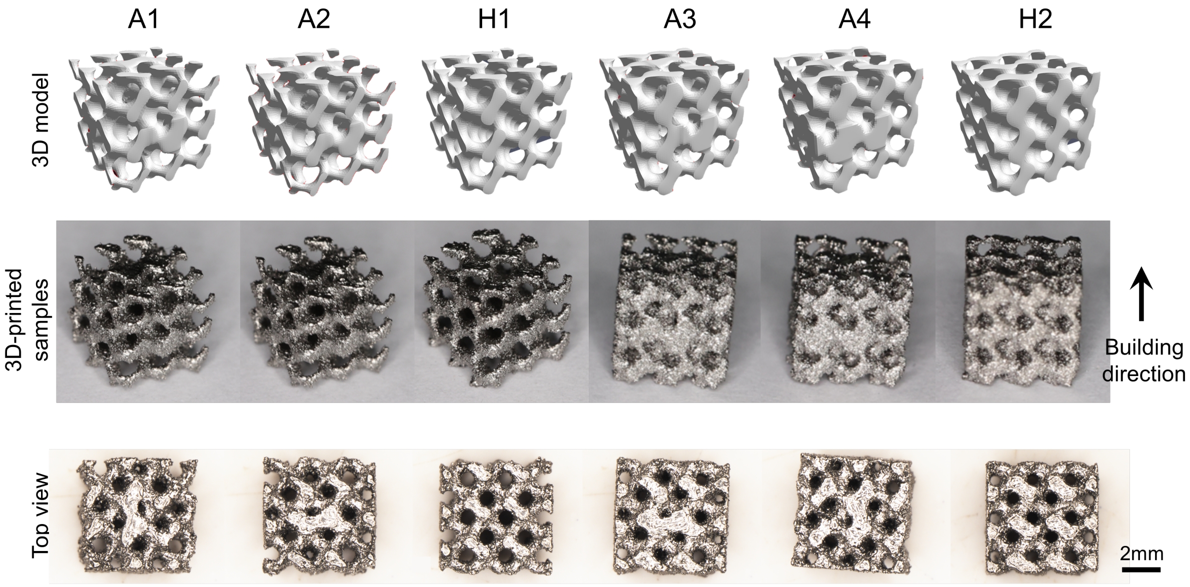

Fig. 16. The camera pictured Ti cubic scaffolds. The 3D model, perspective view, and top view of ML designs (A1-A4) and expert designs (H1 and H2).

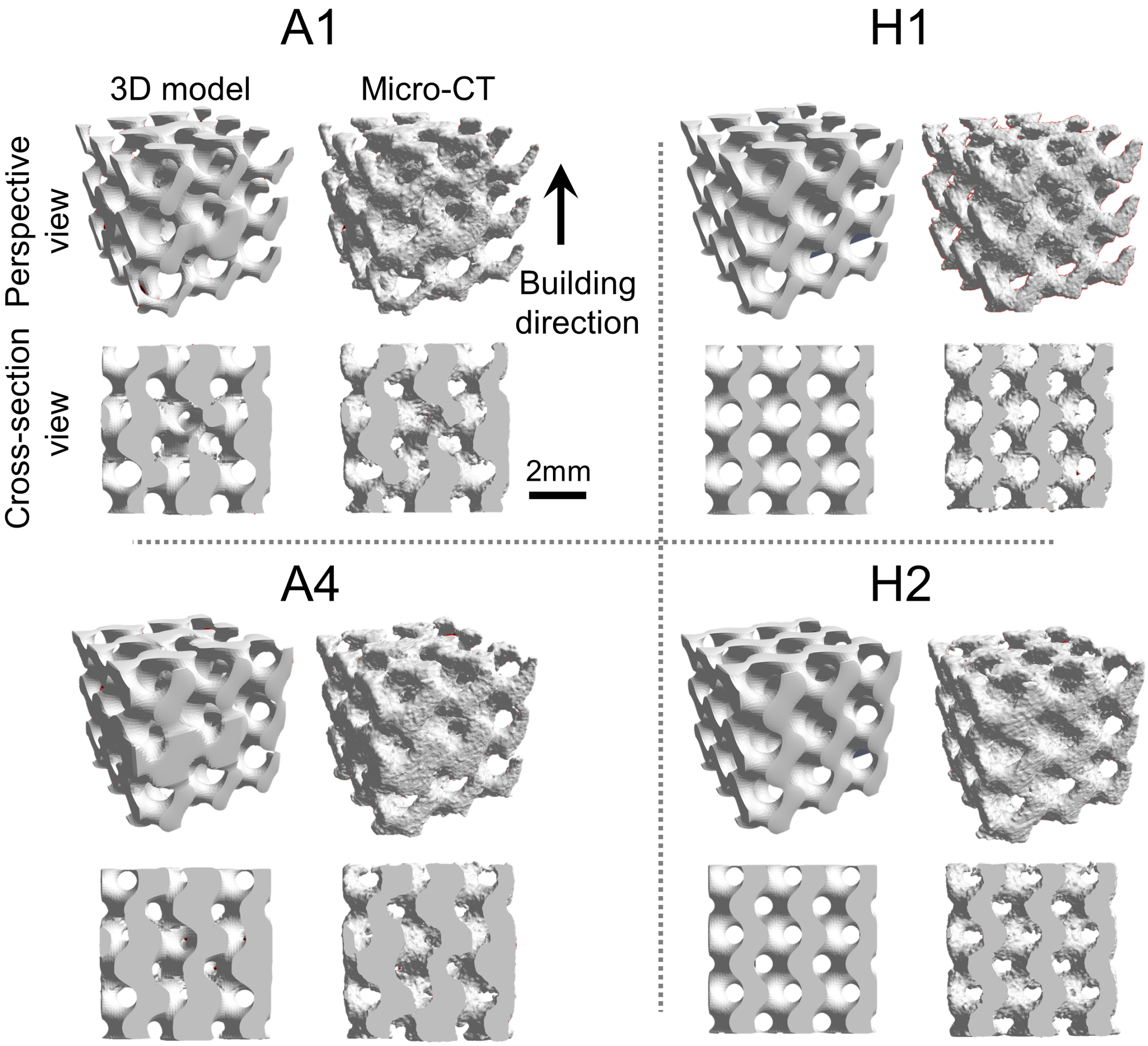

Fig. 17. The micro-computed tomography (Micro-CT) and 3D model of the Ti cubic scaffolds. ML designs (A1 and A4) and expert designs (H1 and H2).

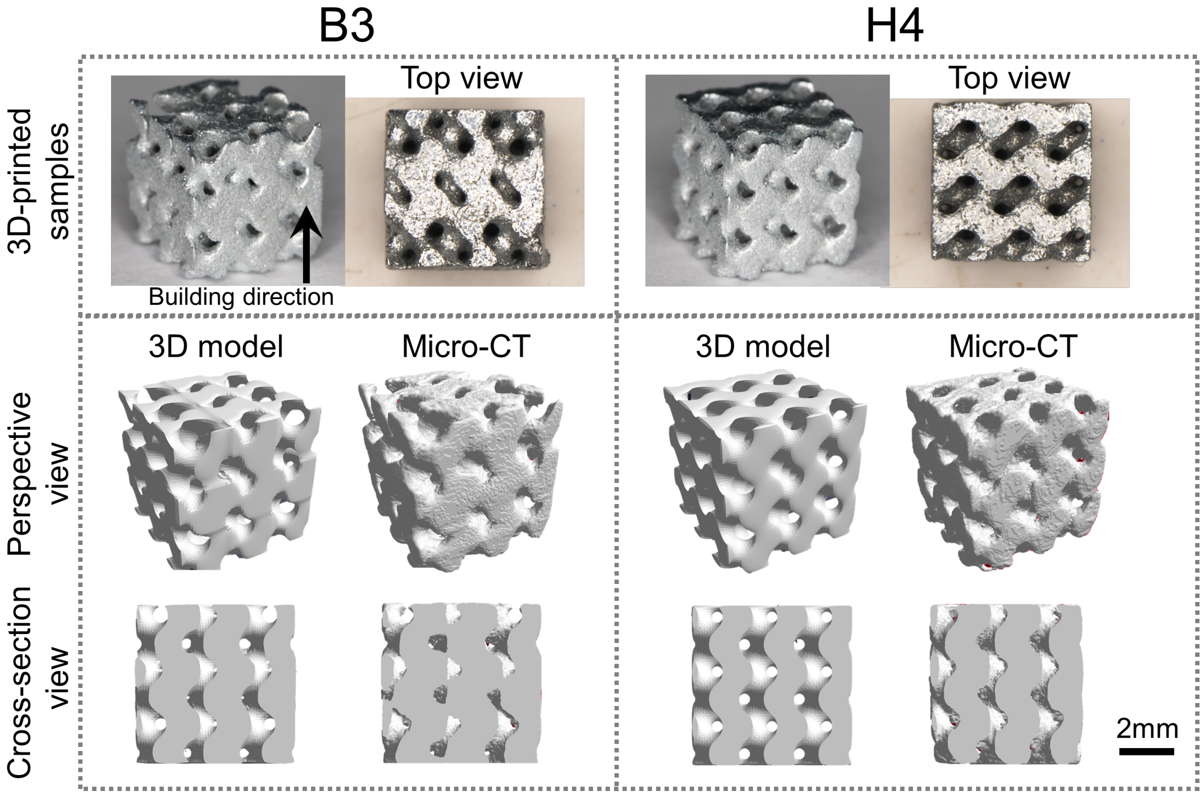

Fig. 18. Characterization of the Zn cubic scaffolds. The pictures, Micro-CT and 3D model of ML design (B3) and expert design (H4).

Table 5 – The actual porosity of scaffolds from Micro-CT characterizes

	A1	H1	A4	H2	B3	H4
3D Model porosity (%)	68.9	72.0	55.7	60.7	39.6	44.0
Real porosity (%)	69.2	72.2	55.4	61.1	34.9	39.2

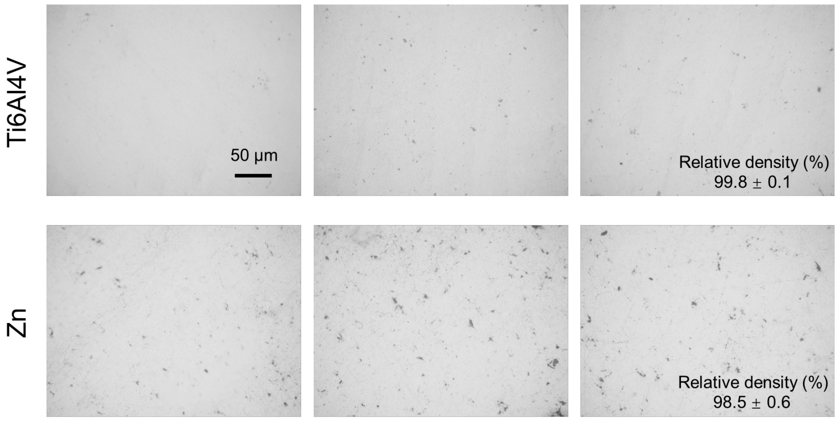

Fig. 19. The cross-section pictures of the Ti and Zn cubic scaffolds. These pictures were used to calculate the relative density of composing struts in cubic scaffolds.

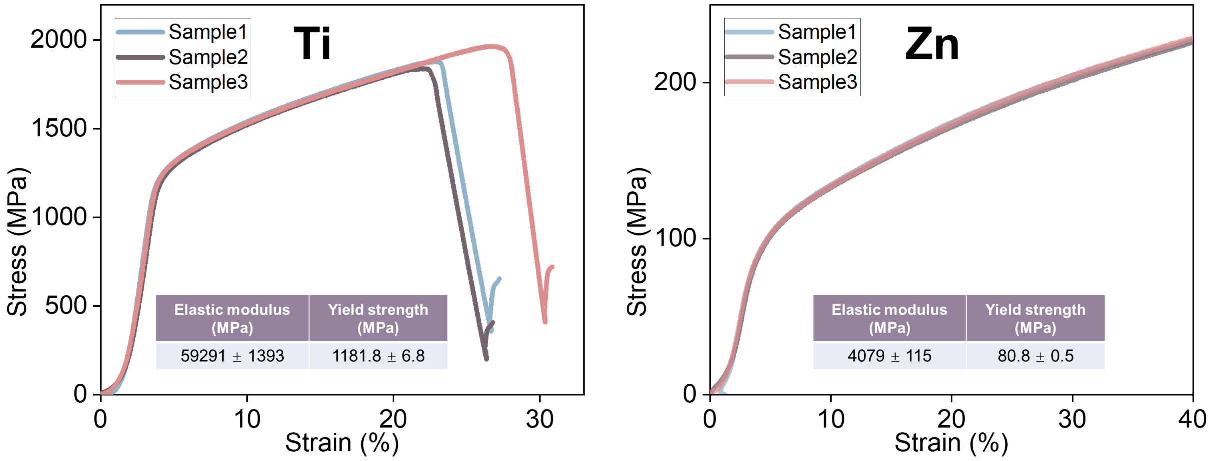

Fig. 20. Experimental strain-stress curves of solid Ti and Zn. These curves are used as benchmarks for the FEM parameter calibrations. In each figure, all stress-strain curves are adjusted in the x-axis direction to make them overlap.

S5. Irregular-shaped scaffolds for bone implants

Fig. 21 shows the design workflow for an irregular-shaped scaffold. We used a $3 * 3 * 9$ raw structure as the starting point. The sub-unit is the ML-designed cubic scaffold. Overall, the whole structure consists of $9 * 9 * 27$ Gyroid units. The scaffold structure was then caved out of the raw materials with the shape matching that of the bones.

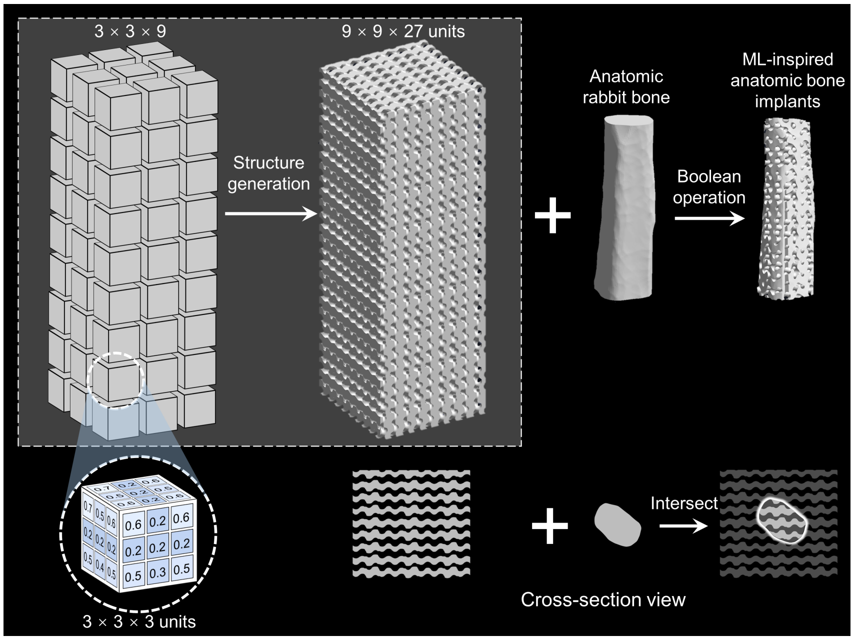

Fig. 21. Pipeline for irregular-shaped scaffold design. We used the $3 * 3 * 9$ raw structure as the starting point, with each sub-unit representing the ML-designed cubic scaffold. The bone-shaped scaffold was then caved out of the raw structure.

The designed bone implant was manufactured and the experimental compression test was performed three times. The resulting strain-stress curves were shown in Fig. 22.

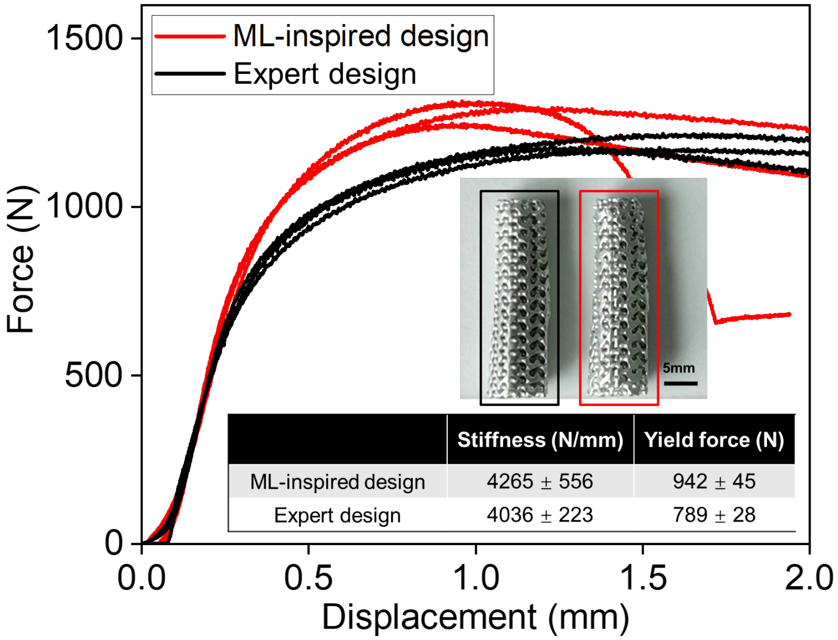

	Stiffness (N/mm)	Yield force (N)
ML-inspired design	4265 ± 556	942 ± 45
Expert design	4036 ± 223	789 ± 28

Fig. 22. Experimental displacement-force curves of bone scaffolds. Three replicas were tested in order to ensure reproducibility. In each figure, all stress-strain curves are adjusted in the x-axis direction to make them overlap.

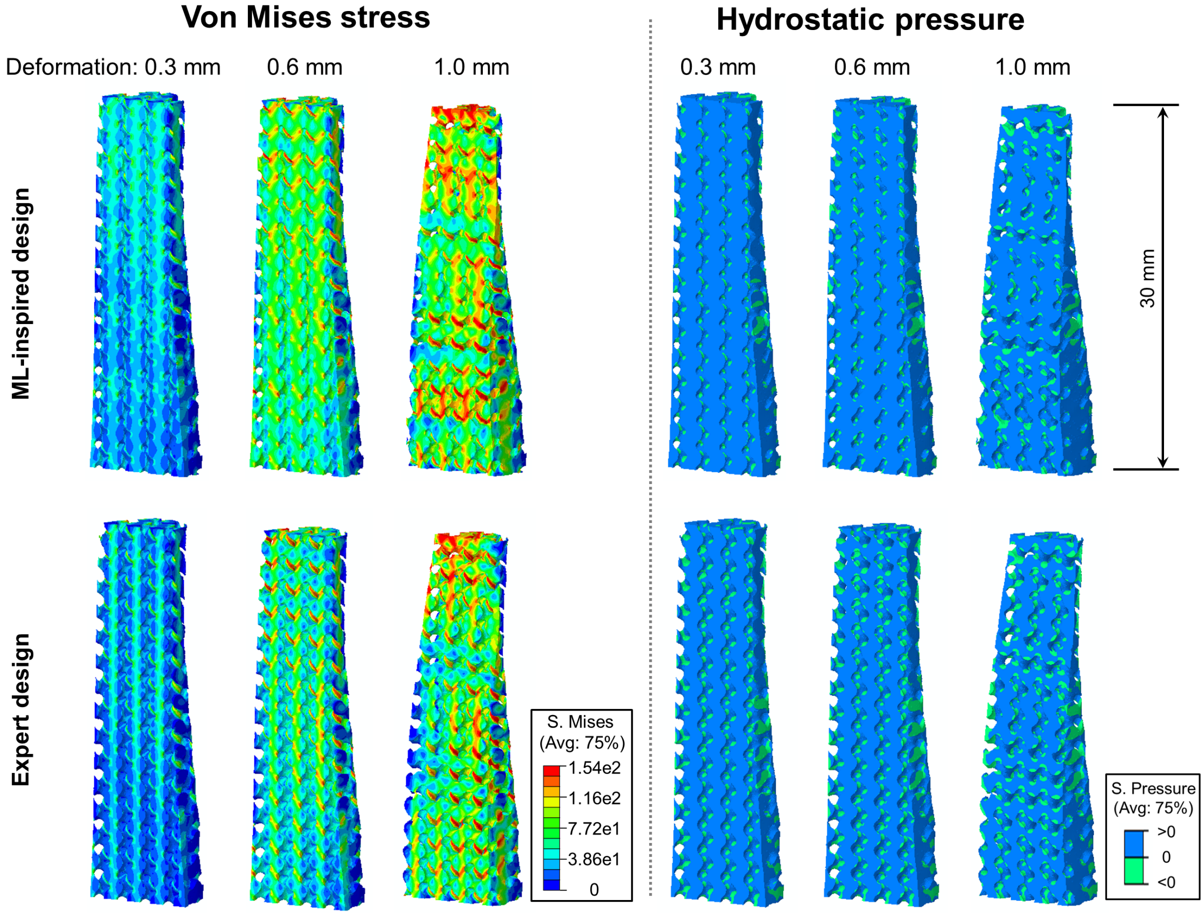

Fig. 23. FEM analysis of the anatomic bone implant. Numerical compression analysis of Von-Mises stress and hydrostatic pressure under 0.3, 0.6, 1.0 mm deformation. The cross-section view of ML-inspired design and expert design is plotted.

References and Notes

1. M. Smith, *ABAQUS/Standard User's Manual, Version 6.9* (Dassault Systèmes Simulia Corp, United States, 2009).